Description Of A Framework And Associated Sensitivity Analysis For Recovery Of Rheological Models And Their Key Parameters Using Multi-Cycle Fault Slip Models

Tobias Köhne[1], Rishav Mallick[1], Mark Simons[1]

[1] Seismological Laboratory, Division of Geological and Planetary Sciences, California Institute of Technology ✉ tkoehne@caltech.edu 👤 www.tobiaskoehne.de

EGU General Assembly 2023

X2.271

EGU23-8837

I. Motivation & Previous Work

- **Constraining the effective rheology of subduction zone megathrusts is crucial** to improve our understanding of the physics of convergent plate boundary deformation (e.g., Bürgmann & Dresen, 2008) — including questions like **how does stress accumulate, release and distribute** during the earthquake cycle, where and how are mountain ranges sustained, how can plate-like tectonics exist, and what does our understanding imply for seismic hazard assessments?
- **Laboratory experiments** have been used to propose constitutive relations of specific rock types at the **micron to meter scale** (e.g., Blanpied et al., 1995; Hirth, 2002; Hirth & Kohlstedt, 2004).
- Postseismic displacement timeseries observations near plate interfaces have since been used to estimate ranges of parameters for such models (e.g., Freed et al., 2012; Agata et al., 2019; Muto et al., 2019; Weiss et al., 2019; Fukuda & Johnson, 2021) although it is unclear if **geodetic evidence** can distinguish between different models at **megathrust scales**.

→ **Longterm goal:**
Identify classes of rheological models that are internally consistent over different phases of the seismic cycle.

- We build on the concepts of Hetland & Simons (2010) and Hetland et al. (2010) that **model interseismic creep in an idealized subduction zone** given a recurring rupture sequence, locked asperity patches, and a rheological model.

→ **Goal for this study:**
Develop a framework to solve for rheological parameters on a simulated, 2D megathrust in a probabilistic inverse sense, with the eventual aim of full 3D analysis of geodetic data in Northern Japan.

II. Method

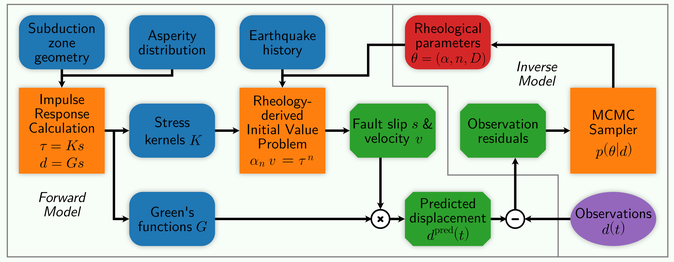

Fig. 1: Workflow schematic. Orange rectangles represent key computational steps. Rounded rectangles represent hyperparameters (kept constant) and regular parameters (to be estimated) in blue and red, respectively. Rectangles with cut corners represent state variables, and the purple ellipse represents the (synthetic) observations. More details about the process on the right.

- **Asperities: predefined regions that only slip coseismically** with known recurrence time and slip amount.
- **Rheology: depth-dependent power-law viscous rheology** $\alpha_n\, v = \tau^n$ (α_n rheological strength term, v slip velocity, τ shear stress, n power-law exponent), appropriate for linear-viscous, power-law viscous, and rate-dependent frictional models (e.g., Montési & Hirth, 2003; Montési, 2004; Mallick et al., 2022).
- **Boundary integral formulation:** $d\tau/dt = K(v - v_p)$ (K stress kernel, v_p plate velocity), initial conditions obtained by spin-up.
- **Markov-Chain Monte-Carlo (MCMC) framework:** maximize the likelihood $p(d|\theta) = \mathcal{N}(d|g(\theta), C_{\text{X}})$, matching the entire timeseries (not a functional fit), yielding the **posterior distribution** $\boldsymbol{p(\theta|d)}$ for parameters $\theta = (\alpha, n)$ using the CATMIP algorithm (Minson et al., 2013) as implemented in the AlTar software.
- **Errors:** observations $d = g(\theta) + e + \epsilon$, corrupted by observation errors e (covariance C_d currently assumed as constant, diagonal matrix) as well as the model errors ϵ (covariance C_p, currently ignored) with $C_{\text{X}} = C_d + C_p$.
- **Effective viscosity:** defined as $\alpha = \alpha_n^{1/n} \cdot v^{1/n-1}$.

V. Viscosity Recovery Comparison

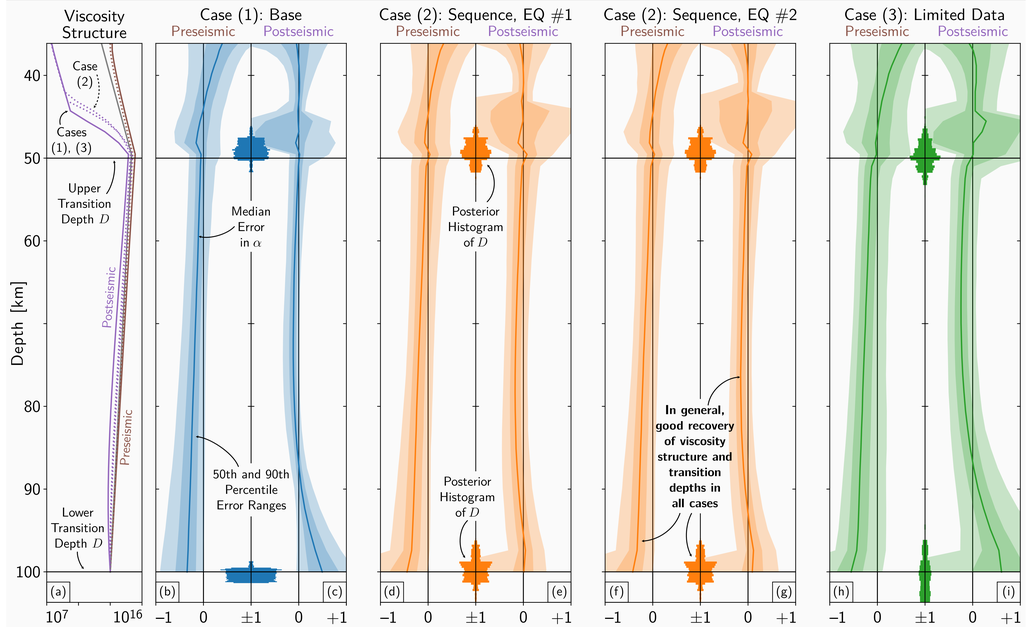

Fig. 5: Comparison of the error in the recovered effective viscosity structure for three selected simulation test cases. The true viscosity structure used in all cases is given in the leftmost panel (a) for the depth range of creeping fault patches. To convert the power-law rheological parameters into an effective viscosity, a velocity has to be assumed. The grey curve uses the plate convergence rate, and the brown and purple curves use the pre- and postseismic fault patch velocities, respectively. The solid lines refer to cases (1) and (3) that only include one observed earthquake, and the dotted lines refer to case (2) where two earthquakes are observed (see Fig. 4). Case (3) only observes the postseismic horizontal displacement starting two weeks after the earthquake, and contains significant uncertainty in the earthquake's assumed coeismic slip amount. In all test cases, the overall plate rate is recovered after the same earthquake cycle length. The other panels (b)–(i) show the errors in the recovered viscosity structure, as well as the recovered transition depths. The blue, orange, and green colors represent test cases (1)–(3), respectively. Panels (b), (d), (f), and (h) correspond to the preseismic apparent viscosity, and panels (c), (e), (g), and (i) to the postseismic one. Within each test case, the colored solid lines show the median error between the logarithm of the recovered viscosity profile and the true values, where $\pm$ 1 refers to an error of one order of magnitude. The light and medium shaded areas around the solid line represent the 90th and 50th percentile ranges, respectively. The dark shaded areas are horizontal histograms for the estimate of the transition depths. Overall, the viscosity structure can be estimated to within half an order of magnitude or better, and transition depths are well contrained. Case (2) shows that observing multiple earthquakes benefits the estimate of the deep postseismic effective viscosity.

VI. Base Test Case (1): Posterior Probability Densities

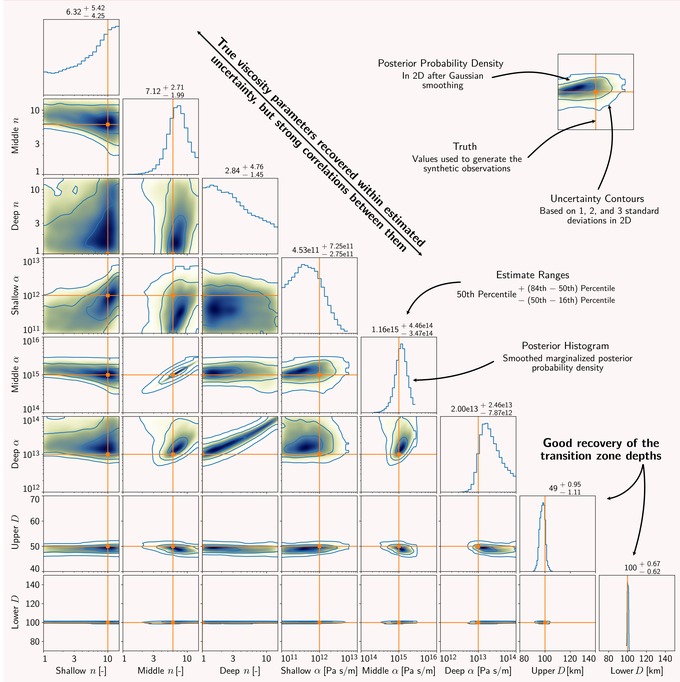

Fig. 6: Corner plot of the posterior covariance matrix for case (1) as approximated by the MCMC inversion process for the eight estimated parameters defining the depth-dependent power-law viscosity structure (see Fig. 5). The figures on the diagonal represent smoothed 1D histograms of the marginalized posterior probability density functions (PDF) for each parameter. The off-diagonal plots are smoothed 2D histograms of the posterior PDF, with contour lines indicating the 1, 2, and 3 standard deviation ranges from the mean. The two transition depths are clearly recovered, with small uncertainties. The rheological parameters α and n are somewhat constrained with strong correlations between them. However, as Fig. 5 shows, the MCMC sampler correctly identifies effective viscosity as the space in which the observations' information is contained. All priors are uniform. Sampling for the rheological parameters is performed in logarithmic space. This test case of 4800 samples with a chain length of 50 completed in 7.25 hours using all 32 threads on 3 CPUs.

III. Model Setup

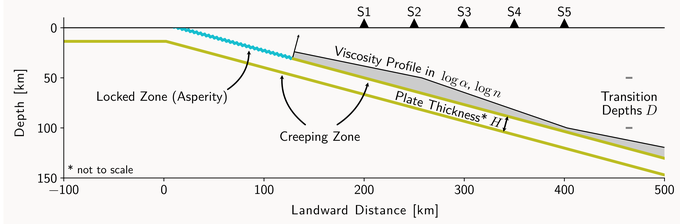

Fig. 2: Model setup of the subduction zone, following the Elastic Subducting Plate Model (ESPM, Kanda & Simons, 2010). Two plate interfaces approximate the downgoing slab, with the upper and lower interface experiencing left- and right-lateral shearing motion, respectively. The location of observers S1–5 (Fig. 4) is given by the black triangles. Over the length of the upper, creeping interface, the rheological parameters α and n vary linearly in logarithmic space, with an upper and lower transition depth D where the slopes change. To ensure viscous coupling of the plate interface with the mantle at depth, the viscous strength is set to a very high value at large depths below the lower transition.

IV. Synthetic Observations

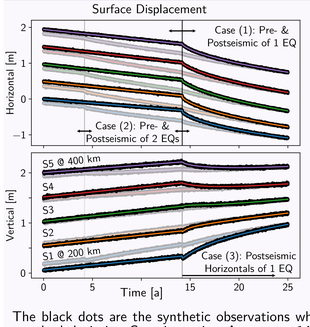

Fig. 4: Simulated surface displacement timeseries used as input for all test cases (see Figs. 5 and 6 for rheological parameters used to create this timeseries). The solid lines are the true timeseries, with colors corresponding to observer location. The labels refer to the names of the stations, with the range of trenchward distances given as well. The black dots are the synthetic observations which include a 1 cm standard deviation Gaussian noise. At approx. 14.2 a (vertical black line), an earthquake occurs and starts a postseismic transient process. The coseismic offset is removed both in this plot, as well as in the observations used in the inference process. Which observations a test case (see Fig. 5) uses is given by the text at the arrows.

VII. Conclusions

- Using probabilistic forward models, the **effective viscosity structure** at depth can be **well recovered**.
- Observing multiple earthquakes and using all data components improves the fit.
- The **high quality of the recovery** even with limited data is likely due to the **importance of our assumptions** (perfect knowledge of fault and elastic structure in the halfspace).
- Next step: extend to real observations in 3D.

References

[1] Agata, R., Barbot, S. D., Fujita, K., Hyodo, M., Iinuma, T., Nakata, R., et al. (2019). *Rapid mantle flow with power-law creep explains deformation after the 2011 Tohoku mega-quake.* Nature Communications, 10(1), 1385.

[2] Blanpied, M. L., Lockner, D. A., & Byerlee, J. D. (1995). Frictional slip of granite at hydrothermal conditions. Journal of Geophysical Research: Solid Earth, 100(B7), 13045–13064.

[3] Freed, A. M., Hirth, G., & Behn, M. D. (2012). *Using short-term postseismic displacements to infer the ambient deformation conditions of the upper mantle.* Journal of Geophysical Research: Solid Earth, 117(B1).

[4] Fukuda, J., & Johnson, K. M. (2021). *Bayesian Inversion for a Stress-Driven Model of Afterslip and Viscoelastic Relaxation: Method and Application to Postseismic Deformation Following the 2011 MW 9.0 Tohoku-Oki Earthquake.* Journal of Geophysical Research: Solid Earth, 126(5).

[5] Hetland, E. A., & Simons, M. (2010). *Post-seismic and interseismic fault creep II: transient creep and interseismic stress shadows on megathrusts.* Geophysical Journal International, 181(1), 99–112.

[6] Hetland, E. A., Simons, M., & Dunham, E. M. (2010). *Post-seismic and interseismic fault creep I: model description.* Geophysical Journal International, 181(1), 81–98.

[7] Hirth, G. (2002). *Laboratory Constraints on the Rheology of the Upper Mantle.* Reviews in Mineralogy and Geochemistry, 51(1), 97–120.

[8] Hirth, G., & Kohlstedt, D. (2004). *Rheology of the Upper Mantle and the Mantle Wedge: A View from the Experimentalists.* In Inside the Subduction Factory (pp. 83–105). American Geophysical Union (AGU).

[9] Kanda, R. V. S., & Simons, M. (2010). *An elastic plate model for interseismic deformation in subduction zones.* Journal of Geophysical Research: Solid Earth, 115(B3).

[10] Mallick, R., Lambert, V., & Meade, B. (2022). *On the Choice and Implications of Rheologies That Maintain Kinematic and Dynamic Consistency Over the Entire Earthquake Cycle.* Journal of Geophysical Research: Solid Earth, 127(9).

[11] Minson, S. E., Simons, M., & Beck, J. L. (2013). *Bayesian inversion for finite fault earthquake source models I—theory and algorithm.* Geophysical Journal International, 194(3), 1701–1726.

[12] Montési, L. G. J. (2004). *Controls of shear zone rheology and tectonic loading on postseismic creep.* Journal of Geophysical Research: Solid Earth, 109(B10).

[13] Montési, L. G. J., & Hirth, G. (2003). *Grain size evolution and the rheology of ductile shear zones: from laboratory experiments to postseismic creep.* Earth and Planetary Science Letters, 211(1), 97–110.

[14] Muto, J., Moore, J. D. P., Barbot, S., Iinuma, T., Ohta, Y., & Iwamori, H. (2019). *Coupled afterslip and transient mantle flow after the 2011 Tohoku earthquake.* Science Advances, 5(9).

[15] Weiss, J. R., Qiu, Q., Barbot, S., Wright, T. J., Foster, J. H., Saunders, A., et al. (2019). *Illuminating subduction zone rheological properties in the wake of a giant earthquake.* Science Advances, 5(12).